J. Fluid Mech. (1986), *vol.* 172, *pp.* 47–61
Printed in Great Britain

An experimental investigation of oscillating flow in a tapered channel

By DONALD P. GAVER, III AND JAMES B. GROTBERG

Department of Biomedical Engineering, The Technological Institute, Northwestern University, Evanston, IL 60201, USA *and*
Department of Anesthesia, Northwestern University Medical School, Chicago, IL 60611, USA

(Received 24 January 1986 and in revised form 5 May 1986)

Oscillating flow in a tapered channel was studied experimentally by observing the deformation of a dye streak within a Plexiglas channel during piston induced, volume-cycled oscillations. The observed steady streaming was compared to theoretical calculations. Both the theoretical and experimental results show bi-directional drift for all frequencies, with characteristics dependent upon the value of the Womersley parameter, $\alpha = b(\omega/\nu)^{\frac{1}{2}}$. For large values of α, e.g. $\alpha > 10$, the fluid near the walls and along the centreline drifted towards the narrow end of the channel, while fluid in an intermediate region drifted towards the wide end of the channel. For small values of α, e.g. $\alpha < 5$, the fluid drifted towards the narrow end at the wall and the wide end of the channel along the centreline. Applications to mass transport in the lung are discussed.

1. Introduction

High-frequency ventilation (HFV) is of interest because of its potential clinical use during surgery and in the intensive-care setting. In contrast to conventional ventilation, which mimics normal breathing, the high-frequency ventilator operates with tidal volumes much smaller than the anatomic dead space at rates of 5–30 Hz. HFV has been used successfully to ventilate dogs (Bohn *et al.* 1980) and humans (Butler *et al.* 1980). In addition, HFV may decrease the risk of barotrauma to the patient, and has been shown to be useful in the care of neonates (Special conference report 1983).

One fluid dynamic feature of HFV is the oscillatory gas flow in the neighbourhood of an airway bifurcation. In this region the axial velocity profiles of inspiration differ from those of expiration, due to the curvature of the airways as well as the taper of cross-sectional area. This asymmetry of velocities leads to steady streaming in the axial direction. Haselton & Scherer (1982) observed such streaming in an experimental investigation of volume-cycled oscillatory flow in a model bifurcation. At lower Womersley numbers, $\alpha \leqslant O(1)$, they found the streaming velocity profiles to be bi-directional and to correlate qualitatively with quasi-steady arguments. Fluid near the walls drifted towards the parent tube (negative drift) while fluid near the centreline drifted towards the daughter tubes (positive drift). For $\alpha \gg O(1)$ there were no conclusive observations or analysis. With the experiments of Scherer & Haselton (1982) it was shown that streaming behaviour can lead to the distribution of non-diffusive particles in a branching tube network model of a bronchial tree. Grotberg (1984) mathematically modelled the region near an airway bifurcation as a tapered channel and studied the volume-cycled flow through this geometry.

Although greatly simplifying the actual airway geometry, this model predicts steady streaming patterns for $\alpha \leqslant O(1)$ that are consistent with the observations of Haselton & Scherer. The predictions for $\alpha \gg O(1)$ differ significantly from the low-frequency case, particularly in the reversal of drift direction near the centreline.

Numerous studies of steady streaming in oscillatory flows have been made. Rosenblat (1959, 1960) and Jones & Rosenblat (1969) studied the streaming behaviour induced by a torsionally oscillated disk, while Riley (1965, 1967) and Stuart (1966) examined the steady streaming flow that exists adjacent to a cylinder oscillating along its diameter. This flow has also been experimentally investigated by Schlichting (1932) and Bertelsen (1974). In addition, streaming appears in oscillating flow along a curved tube in the theory of Lyne (1970) and experiments by Bertelsen (1974). Hall (1974) presented a theory of pressure-cycled oscillatory flow within a tapered tube. His results show uni-directional streaming toward the wide end of the tube, indicating that the impedance to flow is greater in the direction of decreasing cross-section than in the opposite direction. For this reason the pressure cycling does not lead to fixed tidal volume oscillations. When fixed tidal volumes are imposed instead of pressure cycling, Grotberg's results indicate the existence of bi-directional drift, and a flow reversal in the core region for $\alpha \gg 1$. This analysis requires a double boundary layer: the Stokes layer, which describes the distance over which rapid variations of the oscillating velocity profile occur; and the drift layer, the distance over which rapid variations in the steady velocity profile occur.

Double boundary layers have been calculated to exist in the oscillating cylinder and disk problems, studied by Stuart and Rosenblat, respectively. The characteristics of these layers, however, have never been accurately measured, although Bertelsen has shown similarity in the experimental behaviour of the outer region of the steady boundary layer of an oscillating cylinder with the predictions of Riley and Stuart. Budwig (1985) also observed the steady and unsteady boundary layers associated with oscillating fluid flow in a tapered tube.

In this study we examine the flow in a tapered channel undergoing volume cycling. The dimensionless governing parameters in this problem are: the axial stroke distance, A, which measures the unsteady axial displacement relative to the channel depth; the lateral amplitude parameter, $\lambda = \epsilon A$, which measures the unsteady lateral displacement; ϵ, the slope of the channel walls; and finally the Womersley number, $\alpha = b(\omega/\nu)^{\frac{1}{2}}$, the ratio of unsteady to viscous effects.

We study the flow in a Plexiglas channel of fixed linear wall taper by varying the piston amplitude, fluid viscosity, and frequency of oscillation, thus varying the parameters A, λ, and α. The fluid motion in each case is examined by the deformation of a tracer dye streak injected into the channel. Theoretical calculations were made of the Eulerian and Lagrangian velocity profiles following the analysis of Grotberg (1984), and extended by numerical calculation of the Lagrangian drift velocity profiles for stroke amplitudes of $O(1)$. These results are then compared with the experimental data.

2. Methods

The experimental apparatus consists of three distinct parts. These are the channel, the drive mechanism, and the fluid measurement systems.

The channel, constructed of $\frac{1}{2}$-inch thick Plexiglas, consists of three sections, two straight sections separated by a tapered section and connected together by flanges.

The interior height of each of these sections is 60 cm. The interior width of the tapered section varies linearly from 3 to 5 cm over a 20 cm distance. The straight sections have internal widths of 3 and 5 cm and are connected smoothly to the tapered section. The straight sections each have a length of 2 ft. A rectangular piston is positioned at the end of the wide parallel-walled section and is driven by a rod connected to the drive mechanism. Leakage around the piston rod is prevented by the use of a moveable seal consisting of a modified air cylinder. The displaced fluid flows through return tubes connected to the wide section behind the piston to the far end of the narrow section. This return tube mechanism serves to equalize the pressure across the piston, as well as eliminating the need for large reservoirs on each side of the channel. By removing the reservoirs the free surface effects are decreased, and pressure fluctuations are due largely to the dynamics of the flow field. A series of flow straighteners consisting of honeycombed aluminium and wire mesh are placed at the narrow end, and a slotted tube is used to smooth the flow entering and exiting the return system. This tube eliminates the eddy shedding that would otherwise occur at the junction of the channel and return flow systems.

The drive mechanism consists of a Bodine series 500 $\frac{1}{8}$-horsepower variable-speed motor, a Boston Reductor 50:1 ratio turndown gear, and a variable amplitude 'Scotch yoke' drive connected to the piston shaft. The drive system translates the rotational motion of the motor assembly into purely translational motion with a frequency equal to the fundamental driving frequency. Any harmonics are due to inaccuracies of machining, and were observed to be of very small magnitude. The amplitude setting of the cam drive has discrete positions, allowing for stroke amplitudes ranging from 0.25 to 1.5 in. in 0.25 in. increments. The complete drive mechanism is mounted to an aluminium platform to isolate the channel from mechanical vibration.

The fluid motion is visualized by injecting a dye streak across the channel so that Lagrangian displacement may be observed. The dye used is a dilute solution of blue dye mixed with water and glycerine to match the fluid density in the channel as closely as possible. Because of imperfect matching and thermal effects, the injection fluid may have a slightly different density from the channel fluid. However, the channel has been designed so that flow conditions are essentially uniform for a wide band of vertical positions. Therefore, buoyancy-induced displacements in the vertical direction will not affect the axial displacements we seek. The displacement recording system is based on a Canon AE-1 camera with a 90 mm macro lens. The camera faces axially along the top of the channel, focused on a grid pattern held in the vertical plane. A beam splitter is placed at a 45° angle between the camera and grid such that the image of the dye streak is visible to the camera. The beam splitter is placed so that the optical path from the camera to the streak is equal to the path from the camera to the grid. Photographs have the image of the streak superimposed upon the image of the grid, and the grid pattern is then used to measure the displacement of various parts of the streak. The camera triggering mechanism allows photographs to be taken at any one or all of four piston positions – the two extreme, and the two mid-points of the piston stroke. Triggering is achieved by a cable release mounted to the cam drive mechanism, with round-head screws on the drive wheel acting as cams to press the cable release and activate the camera. This system ensures that the piston is in the same part of the piston stroke each time a photograph is taken. After each photograph, an auto-winder advances the film in the camera. Figure 1 is a schematic diagram of the apparatus and measurement systems.

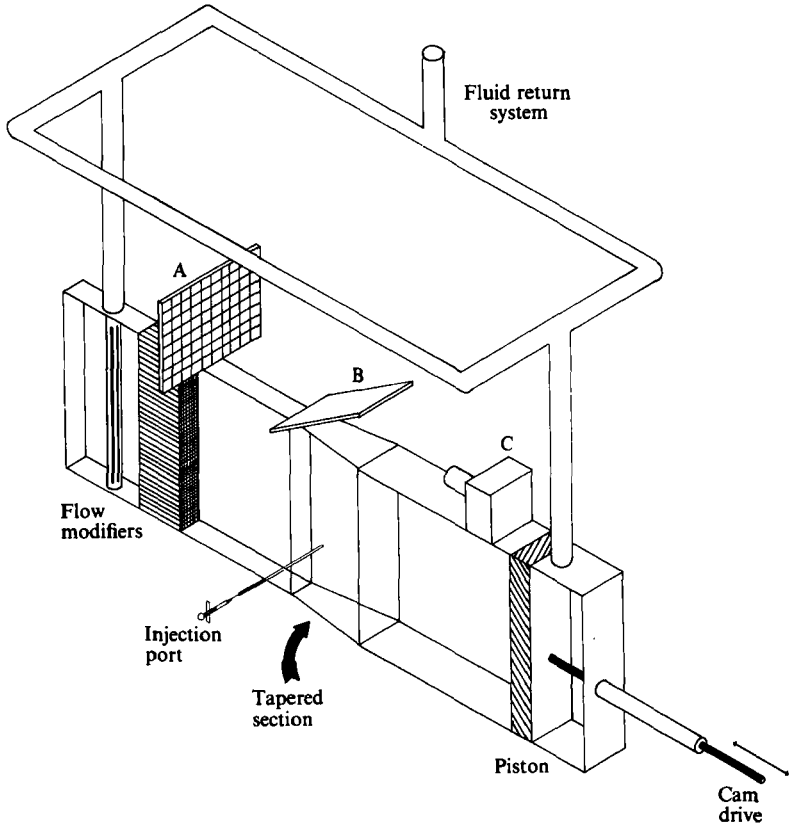

FIGURE 1. Schematic of apparatus. A is the measurement grid, B is the beam splitter, and C is the camera.

The experiments in this study were designed to vary the values of the dimensionless parameters $\alpha = b(\omega/\nu)^{\frac{1}{2}}$, the dimensionless frequency, and $\lambda = \epsilon A$, the lateral amplitude parameter. We performed experiments with mixtures of water and glycerine as the fluid, allowing the viscosity to be changed between experiments. The viscosity was varied between $\nu = 0.01$ cm^2/s and $\nu = 0.10$ cm^2/s. By changing either the viscosity or the oscillation frequency a wide range of α was experimentally available. The tapered section has a linear taper with a slope of $\epsilon = 0.05$, and the representative half-width of the channel was chosen to be the half-width at the dye injection port, $b = 2.0$ cm. Experiments were conducted with piston amplitude oscillations of $L = 1.5$ in. and $L = 1$ in. The characteristic displacement length for the experimental configuration is defined as $d = V/(2bH)$, where V is the stroke volume, b is the half-width, and H is the height of the channel. Since the stroke volume may be found by $V = WHL$, where W is the width of the piston, the representative amplitude of the piston stroke is $WL/(2b^2)$. The experiments in this investigation have characteristic amplitudes of $A = 2.38$, and $A = 1.59$, and a range of α of $3 < \alpha < 25$.

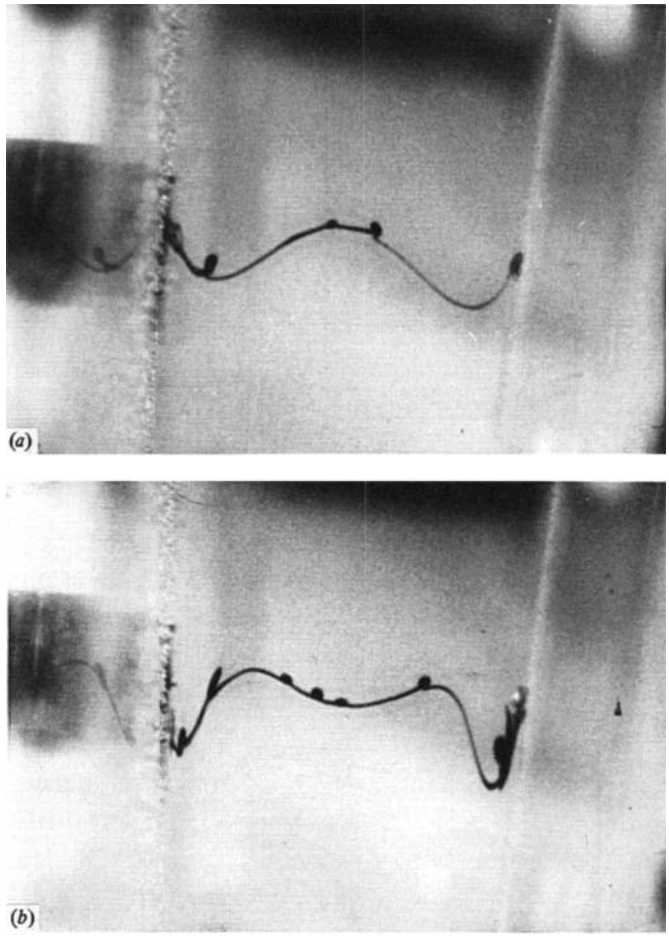

FIGURE 2. Characteristic deformation profile after an integral number of oscillations. $A = 1.59$, $\epsilon = 0.05$. (*a*) $\alpha = 3.8$; (*b*) $\alpha = 17.4$.

3. Results

The data collected during each experiment consist of a series of photographs showing the progression of a dye streak from its initial position as a straight line to the deformed profile that exists after each stroke. Examples of streak deformations after an integral number of piston oscillations for different values of α are shown in figure 2. Figure 2(*a*) shows a streak deformation typical of values of $\alpha < 7$, while figure 2(*b*) shows a streak deformation typical of values of $\alpha > 10$. For intermediate values of α, the profile is in transition between the low- and high-frequency characteristic profiles.

The lengths $W1^*$ and $W2^*$, as shown in figure 3, have been specified as characteristic of the streak's deformation, and may be used for comparison between the experimentally discovered deformation profiles and the profiles determined by theoretical calculation. Figure 3 defines $W1^*$ and $W2^*$ for a streak typical of high-frequency oscillations; for low-frequency oscillations $W2^*$ equals zero, leaving $W1^*$ to describe the streak deformation.

To quantify the rate of steady streaming, the rate of increase of $W1^*$ and $W2^*$ is

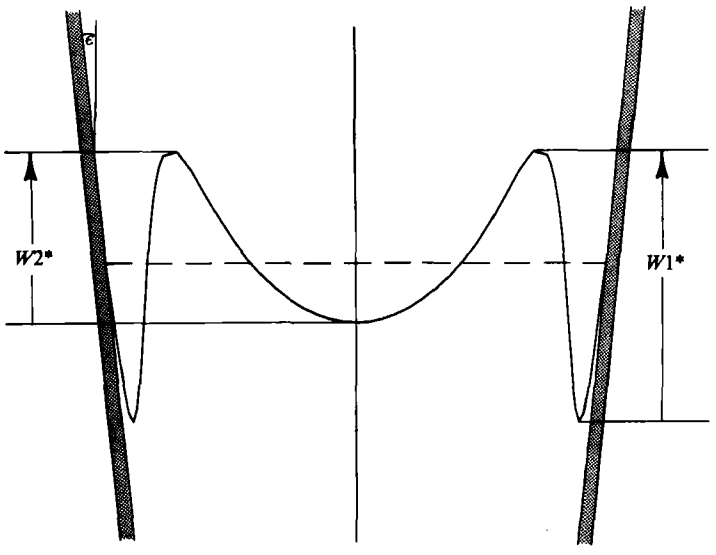

FIGURE 3. Streak deformation profile showing the definitions of $W1^*$ and $W2^*$.

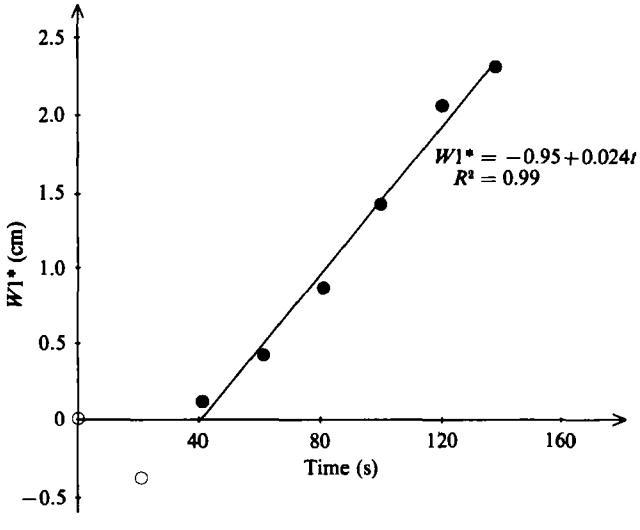

FIGURE 4. An example of the selection steady-state onset time and regression through the steady-state regime. Here an open circle represents data from the start-up transient, and the darkened circles represent the steady-state points. In this experiment $A = 2.38$, $\alpha = 14$, $\epsilon = 0.05$.

determined from measurements of sequential streak deformations and the period of oscillation. Since the initial deformation profiles in the high-frequency experiments show transient start-up behaviour instead of the desired steady-state response, it is necessary to analyse the data with the aim of extracting the steady-state deformation growth rate. This data analysis also helps minimize errors induced by triggering inaccuracies.

To find the steady-state response of the flow, the values of $W1^*$ and $W2^*$ are examined versus time. For example, $W1^*$ is measured at each cycle beginning with start-up and plotted as in figure 4. A least-square linear regression is made of each grouping of four neighbouring points. The slopes of these regressions are compared

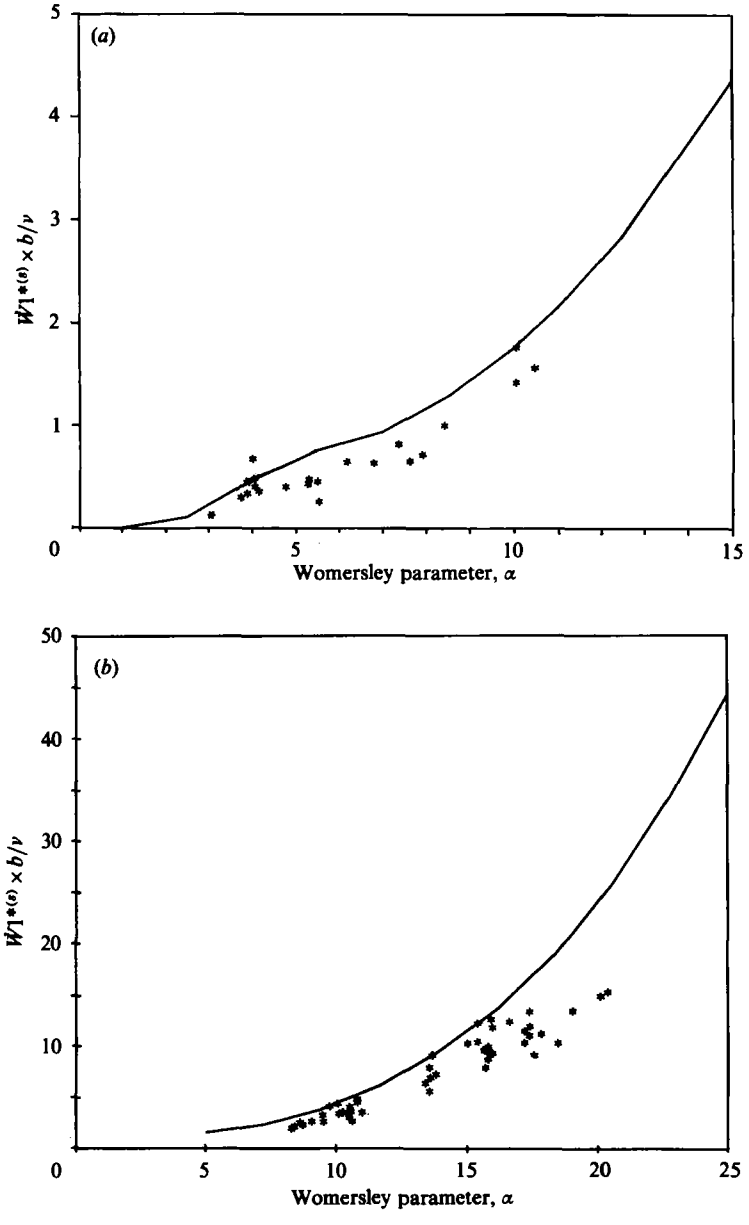

FIGURE 5(*a*, *b*). For caption see next page.

to one another by taking the last three slopes, in time, and determining their average value and variance. The slopes of these regression curves are accepted as being effectively constant if the variance of their values is less than 15% of their average value. If the slopes pass this variance test, an additional slope, moving sequentially towards the beginning of the experiment, is added into the average and variance calculations while dropping the last value, in time, that had been used in the previous calculation. The variance criterion is then tested again, and the procedure repeated until either all of the data points have been tested, or the variance test is failed. The time corresponding to the last accepted value of the slope is then selected as the onset

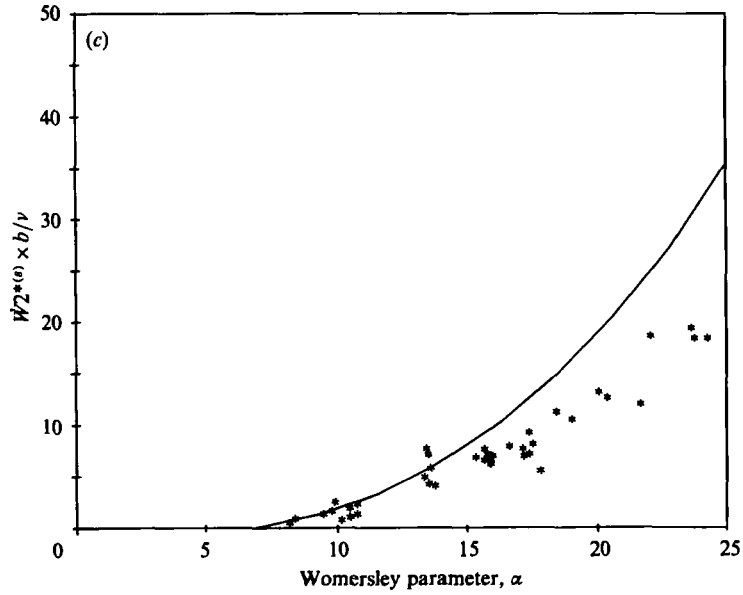

FIGURE 5. Streaming velocity *vs.* α. Asterisks denote the experimental points, and the solid lines represent the results of the Lagrangian displacement calculations. (*a*) $A = 1.59$, $\epsilon = 0.05$; (*b*) $A = 2.38$, $\epsilon = 0.05$; (*c*) $A = 2.38$, $\epsilon = 0.05$.

time of the steady-state behaviour. Once the steady-state onset time is determined, the data within the steady-state regime are fit with a least-square linear regression curve. Finally, the experiment is accepted as valid only if the regression coefficient, R^2, of this regression is greater than 0.98. It is the slope of this regression that corresponds to the growth rate of the deformation characteristic, and is symbolized by $\dot{W}1^{*(s)}$ and $\dot{W}2^{*(s)}$, the dimensional steady growth rate of $W1^*$ and $W2^*$, respectively. An example of the data analysis method is shown in figure 4, indicating the selection of the steady-state onset time and the least-square regression of the steady-state data.

The experimental results of $\dot{W}1^{*(s)} \times b/\nu$ versus α for a dimensionless stroke amplitude of $A = 1.59$ are shown in the data points of figure 5(*a*). Figure 5(*b*) and (*c*) shows the results of experiments of $\dot{W}1^{*(s)} \times b/\nu$ and $\dot{W}2^{*(s)} \times b/\nu$ versus α. respectively, for a dimensionless stroke amplitude of $A = 2.38$.

4. Theory

The fluid-flow problem is formulated in the same manner as Grotberg (1984), with the flow confined between symmetrically tapered walls. The equations of motion and boundary conditions are scaled using the dimensionless variables

$$u = \frac{u^*}{U}, \quad \epsilon v = \frac{v^*}{U}, \quad P = \frac{P^*}{\rho U^2}, \quad t = \omega t^*, \quad x = \frac{\epsilon x^*}{b}, \quad y = \frac{y^*}{b},$$

where b is the half-width of the channel at $x = 0$, V is the tidal volume, d is a measure of the fluid displacement length,

$$d = \frac{V}{2b^2},$$

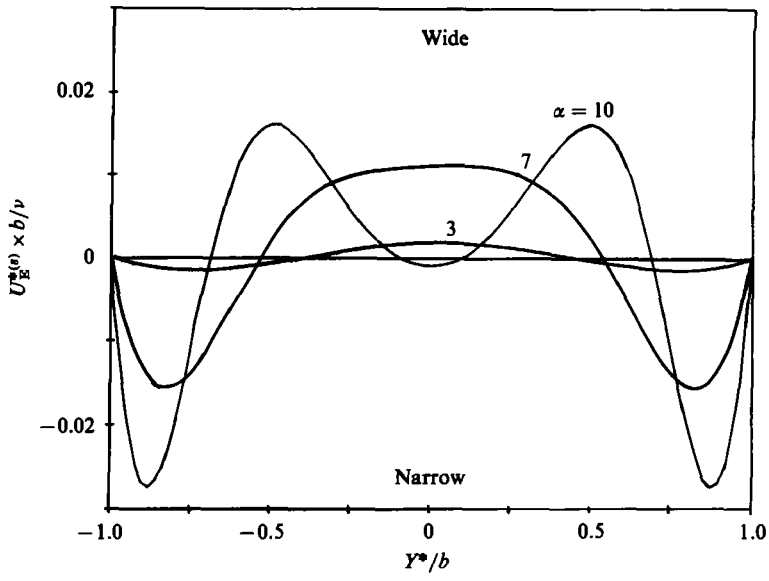

FIGURE 6. Theoretically determined steady Eulerian velocity profiles. $A = 0.25$, $\epsilon = 0.05$, $\alpha = 3$, 7, and 10.

U represents the velocity amplitude,

$$U = \omega d,$$

and ϵ is the slope of the channel walls, assumed to be small. The stream-function equation, neglecting terms of $O(\epsilon^2)$, is found,

$$\alpha^2 \psi_{yyt} - \psi_{yyyy} + \alpha^2 \lambda (\psi_y \psi_{xyy} - \psi_x \psi_{yyy}) = 0,$$

where the dimensionless parameters of this problem are

$$A = \frac{d}{b}, \quad \alpha^2 = \frac{\omega b^2}{\nu}, \quad \lambda = \epsilon A.$$

4.1. *Eulerian velocity solution*, $\alpha < O(1)$

The first- and second-order approximate solution of the stream-function equations are found using a regular perturbation method based upon the small parameter λ,

$$\psi(x, y, t) = \psi_0(x, y, t) + \lambda \psi_1(x, y, t) + O(\lambda^2).$$

Briefly, the solution is of the form

$$\psi_0(x, y, t) = (a_0(x) \sinh(\sigma y) + b_0(x)\, y)\, \mathrm{e}^{it} + \text{c.c.}, \tag{4.1}$$

and

$$\psi_1(x, y, t) = a_1(x, y) + b_1(x) + c_1(x)\, y^3 + (d_1(x, y) + e_1(x)\, y + f_1(x) \sinh(\gamma y))\, \mathrm{e}^{2it} + \text{c.c.}, \tag{4.2}$$

where a_0, b_0, a_1, b_1, c_1, d_1, e_1, and f_1 are found by satisfying the boundary conditions and constant stroke volume condition as outlined by Grotberg. This analysis shows that $\lambda^2 \psi_2$ may be greater than $\lambda \psi_1$ if $\alpha^2 \lambda \ll 1$, and therefore the stream-function

solution presented is only guaranteed to be valid for values of $\alpha^2\lambda \ll 1$. We shall see that our experimental results show this restriction to be too severe in this application.

From the stream-function solutions ((4.1) and (4.2)) it can be seen that to $O(1)$ the stream-function oscillates at the fundamental frequency. The $O(\lambda)$ solution, ψ_1, exhibits the non-linear behaviour of the flow, possessing both an unsteady component of twice the fundamental frequency and a steady component. The steady component of the $O(\lambda)$ solution leads to the steady bi-directional streaming behaviour. Representative Eulerian steady streaming velocity profiles are shown in figure 6 for values of the dimensionless frequency, α, equal to 3, 7, and 10 for $A = 0.25$, $\epsilon = 0.05$, and $x = 0$. From these profiles it is evident that the streaming behaviour changes both in magnitude and form with α. In particular, the profiles display a drift boundary layer near the wall which is much thicker than the Stokes layer by a factor $1/\lambda$ according to Grotberg (1984). In addition, the centreline velocity changes from positive to negative in the vicinity of $\alpha = 8.0$.

4.2. *The Lagrangian velocity*

The trajectory of a non-diffusive contaminant is found from the Lagrangian description of the velocity field. This behaviour may be important to the understanding of particulate deposition in the lung, as well as the immediate use of correlating the theoretical and experimental results of this study.

For small amplitude oscillations the Lagrangian velocity field was found analytically by Grotberg (1984). For large amplitude oscillations a numerical evaluation is used to yield the correct Lagrangian profiles. We use a fourth-order Runge–Kutta routine to integrate the equations

$$\frac{\mathrm{d}\boldsymbol{X}}{\mathrm{d}t} = \boldsymbol{u}(\boldsymbol{X}, t), \tag{4.3}$$

over one oscillation cycle with an initially defined streak position. Here $\boldsymbol{u}(\boldsymbol{X}, t)$ is the Eulerian velocity to $O(\lambda)$ at $\boldsymbol{x} = \boldsymbol{X}$ at time t, and $\boldsymbol{X} = \boldsymbol{X}(\boldsymbol{X}_0, t)$ is the position of a particle whose position was $\boldsymbol{X}_0$ at time t_0. To improve the accuracy of this calculation, the integration was completed with 10 and 20 steps per oscillation cycle, and then a linear Richardson's extrapolation method was used to estimate the profile for zero step size. These deformation profiles were then used for comparison of the analytical and experimental results by dividing the displacements by the dimensionless period, 2π, and thus determining the steady streaming velocities.

Lagrangian velocity profiles for A equal to 2.5, ϵ equal to 0.05 and values of α equal to 3, 7, and 10 are shown in figure 7 for a streak of initial position at $x = 0$. To compare the experimental results with the theoretical calculations, the Lagrangian deformation profiles are calculated by numerical integration of (4.3) for amplitudes equal to those of the experiments and a range of α spanning the experimental values. From the calculated profiles the characteristic deformation lengths $W1^*$ and $W2^*$ are found and their velocities determined by division of the dimensionless period. For comparison with the experiments, both the experimental and theoretical deformation velocities were rescaled by the velocity b/ν. The solid lines in figure 5(*a*), (*b*) and (*c*), represent these solutions.

Table 1 compares the magnitude of the experimental parameters with the range of values necessary for the guaranteed validity Lagrangian drift velocity profiles as determined by the numerical evaluation of (4.3). The experimental parameters are all in the correct range with the exception of α, in which case the experimental range

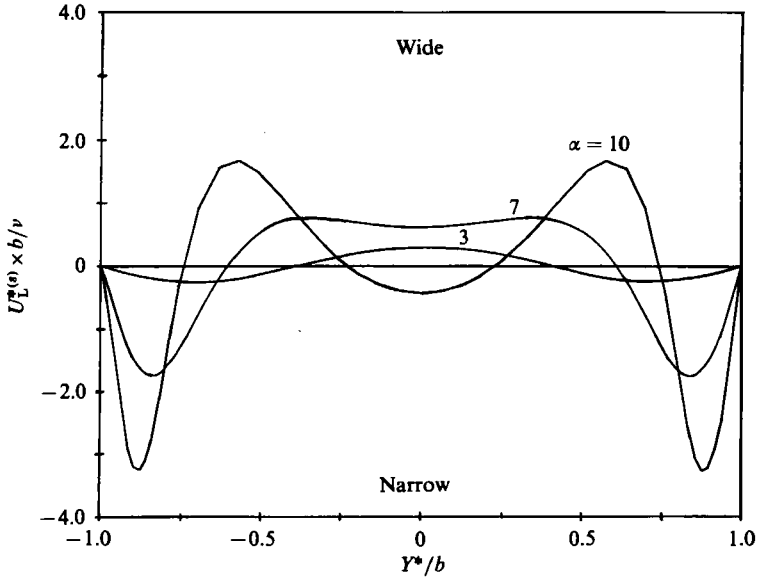

FIGURE 7. Numerically calculated steady Lagrangian velocity profiles. $A = 2.5$, $\epsilon = 0.05$, $\alpha = 3$, 7, and 10.

Parameter	Theoretical approximation	Experimental value
ϵ	$\epsilon \ll 1$	$\epsilon = 0.05$
A	$A \approx O(1)$	(i) $A = 1.58$
		(ii) $A = 2.38$
$\lambda = \epsilon A$	$\lambda \ll 1$	(i) $\lambda = 0.079$
		(ii) $\lambda = 0.119$
$\alpha = b(\omega/\nu)^{\frac{1}{2}}$	$\alpha \approx O(1)$	(i) $3 < \alpha < 11$
		(ii) $8 < \alpha < 21$

TABLE 1. Comparison of the theoretical assumptions of parameter magnitudes with those used in the experiments in this study

is beyond that acceptable for exact comparison of the theoretical and experimental results.

Figure 8(*a*) shows the dependency of $\dot{W}1^{*(s)} \times b/\nu$ upon stroke amplitude for values of α equal to 3, 7, and 10. The dependency of $\dot{W}2^{*(s)} \times b/\nu$ on stroke amplitude for $\alpha = 10$ is shown in figure 8(*b*). In these figures the values for $A < 0.8$ are determined by the analytical solution of the Lagrangian velocity profiles, and the values for $A > 0.8$ were found by the numerical evaluation of (4.3).

5. Discussion

The results of the experimental investigation of oscillating flow in a tapered channel show a high degree of similarity with the corresponding theory. This is especially evident in the comparison of the dye streak deformation profiles and the numerically calculated profiles. Of particular interest is the direction in which the

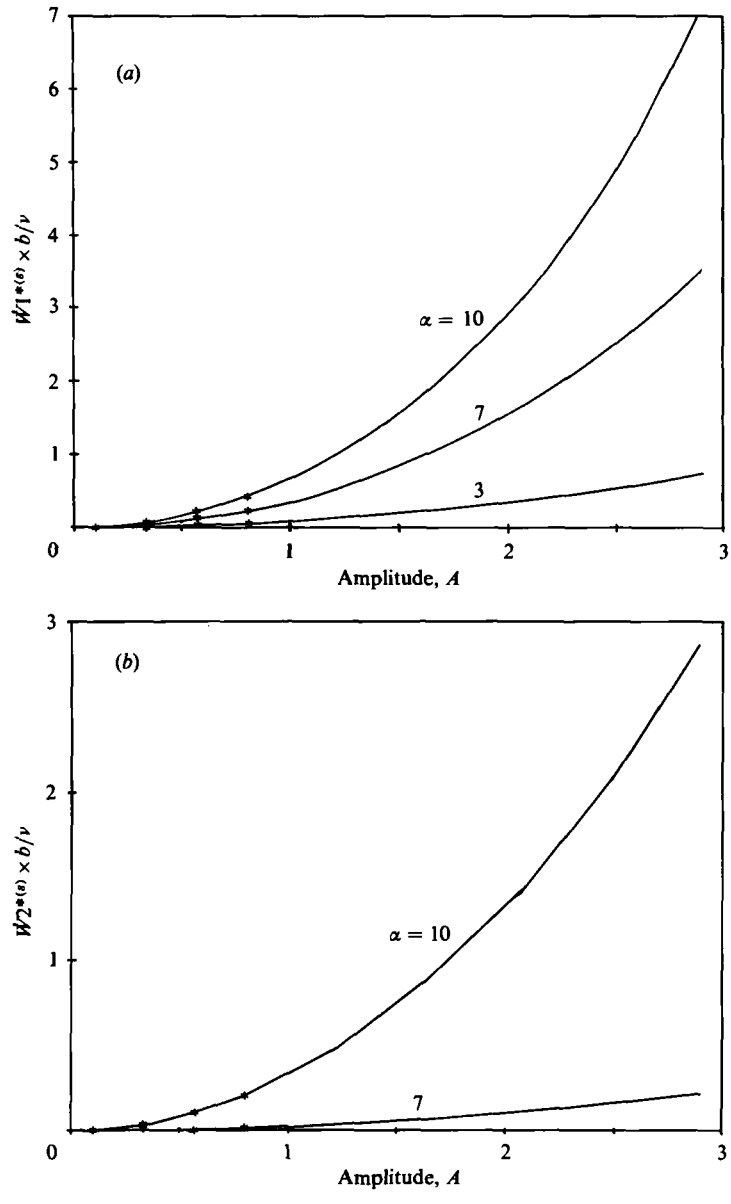

FIGURE 8. Streaming velocity *vs.* amplitude, A, for $\alpha = 3$, 7 and 10. Asterisks represent the analytical calculations, a solid line represents the results of the numerical evaluation of the Lagrangian displacements.

particles stream, and the changes in direction that occur with α. This behaviour is not predicted by the quasi-steady theory proposed by Haselton & Scherer (1982), and has previously not been observed.

Examining the more exact relationship between the theoretical predictions and experimental observations shown in figure 5 (*a–c*), we see that although the theoretical results are not exact, they show a strong correlation with the experimental results. In general, all experimentally determined velocities are less than the corresponding theoretical results. This discrepancy may be due to fluid circulation within the finite

length channel, a feature neglected by the theory. In addition, the oscillating fluid is only partly within the tapered boundaries because of the straight sections. Consequently, the overall tendency for drift is somewhat reduced from the idealized theory. In figure 5(*a*) the experimental results mimic the general theoretical dependency on α. In particular, both the experimental and theoretical results show $\dot{W}1^{*(s)} \times b/\nu$ as monotonically increasing in α with similar slopes. The similarity is especially evident by the mutual appearance of a plateau in the range of α between 5 and 10. Figure 5(*b*) and (*c*) also show a good correspondence between theory and experiment. Both $\dot{W}1^{*(s)} \times b/\nu$ and $\dot{W}2^{*(s)} \times b/\nu$ show remarkable agreement for $\alpha < 13$, while the behaviour at $\alpha > 13$ shows a divergence in which the theoretical predictions are uniformly greater than the observed behaviour.

The high-frequency results, characterized by figure 2(*b*), show bi-directional drift with rapid variations of the deformation profile within the drift layer near the wall. Such a layer is not evident in the low-frequency experiments, characterized by figure 2(*a*). The creation of the drift boundary layer at large values of α is one of the most interesting features of the flow studied here. It is the genesis of this layer than leads to the reversal of flow in the centre region, as can be seen from the $\alpha = 7$ curves in figures 6 and 7. This behaviour may be observed in Haselton & Scherer's Y-tube experiments. For low frequencies a bolus of dye placed near the carina can be seen to propagate towards the parent tube near the wall, and towards the daughter tube near the centre. For high-frequency experiments a jet in the direction of the parent tube is evident near the wall, and in the centre the fluid velocity has reversed from the low-frequency case, and is now in the direction of the parent tube. Between these two layers there seems to be a narrow region of flow towards the daughter tubes.

As discussed above, the asymptotically determined Eulerian velocity field may only be guaranteed valid for $\alpha^2 \ll 1/\lambda$. For the experiments represented in figure 5(*a*), the calculations may only be valid for $\alpha \ll 3.5$. In addition, the calculations represented in figure 5(*b*) and (*c*) may only be valid for values of $\alpha \ll 3.0$. It is evident, however, that there is close agreement with the experimental results beyond these limits of α. This result suggests that the analytical solutions remain accurate for values of α greater than expected.

For values of $\alpha \gg 1$ a similar perturbation method could be used to derive a velocity field to compare to these experiments. The solution for $\alpha \gg 1$ in Grotberg (1984) cannot be directly compared to these experiments, however, since it assumes a parabolic wall shape, while experiments in this study were completed in a channel with a linear taper. Although that solution is not an exact representation, it does exhibit a number of features observed during the experiments. In particular, the singular perturbation analysis shows a drift layer near the wall with peaks in opposite directions, one adjoining the wall with a velocity towards the narrow end of the channel followed by a peak with velocity in the direction of increasing width. In addition, there is a distinct core region in the centre of the channel. This behaviour is evident in the experimental results.

Figure 8(*a*) and (*b*) shows the behaviour of $\dot{W}1^{*(s)} \times b/\nu$ and $\dot{W}2^{*(s)} \times b/\nu$ versus dimensionless amplitude, A. From the analytic solution the dependency for small values of A is seen to be A^2. For values of $A > 1$ this amplitude dependence continues as is indicated by the solid lines in figure 8(*a*) and (*b*). This result is important because it indicates that the efficiency of streaming as a convective mechanism increases with the square of stroke volume. In fact, this result is in agreement with the results of Tarbell, Ultman & Durlofsky (1982) who, in experiments of oscillating flow in a branching network of tubes, found the efficiency of transport of a non-

diffusive dye to be proportional to $V^{1.82}$. Exact comparison cannot be made, since the experiments on branching networks use circular tubes and the cross-sectional increase in area is abrupt, with an increase of 100 % at each bifurcation.

In this study we have examined Lagrangian displacements of a dye streak due to oscillatory flow in a tapered channel. The purpose here was to isolate one of the features of oscillatory flow in the region of a tube or airway bifurcation where the cross-sectional area increases. These results are of direct use for understanding transport of non-diffusive substances such as airborne particulates. The transport of diffusible gases such as O_2 and CO_2 in this model may be determined by inserting the velocity field derived by Grotberg (1984), and verified in these experiments, into the convection–diffusion equation, and solving the boundary-value problem. The corresponding convection–diffusion system for a tapered tube has been solved by Godleski & Grotberg (1985) who show that the area expansion affects transport of diffusible substances primarily by modifying the interaction of axial convection with diffusion across streamlines. The role of steady streaming was small, of $O(\epsilon^3)$, but could be much larger if the posed end concentrations were radially varying rather than uniform. This more difficult problem remains to be investigated.

This work was supported by NIH grant HL/GM-30574 and NSF Presidential Young Investigator Award MEA-8351494 in conjunction with General Motors Corporation, G. D. Searle, and Inland Steel. We are grateful for the technical assistance of Ms Ann Brennan, Mr Douglas Kerns, Professor Lyle Mockros, and Professor Noam Gavriely.

REFERENCES

Bertelsen, A. F. 1974 An experimental investigation of high Reynolds number streaming generated by oscillating cylinders. *J. Fluid Mech.* **64**, 589–597.

Bertelsen, A., Svardal, A. & Tjotta, S. 1973 Nonlinear streaming effects associated with oscillating cylinders. *J. Fluid Mech.* **59**, 493–511.

Bohn, D. J., Miyasaka, K., Marchak, E. B., Thompson, W. K., Froebe, A. B. & Bryan, A. C. 1980 Ventilation by high-frequency oscillation. *J. Appl. Physiol.: Respirat. Environ. Exercise Physiol.* **48**, 710–716.

Budwig, R. S. 1985 Two unsteady heat transfer experiments: I. In grid-generated isotropic turbulence; II. In laminar oscillatory flow in straight and conical tubes. Ph.D. thesis, Johns Hopkins University, Baltimore.

Butler, W. J., Bohn, D. J., Bryan, A. C. & Froese, A. B. 1980 Ventilation by high frequency oscillation in humans. *Anesth. Analg.* **59**, 577–584.

Grotberg, J. B. 1984 Volume-cycled oscillatory flow in a tapered channel. *J. Fluid Mech.* **141**, 249–264.

Godleski, D. A. & Grotberg, J. B. 1985 Mass transport and oscillatory flow in tapered tubes. *Bull. Am. Phys. Soc.* Ser. II, **30**, 1696.

Hall, P. 1974 Unsteady viscous flow in a pipe of slowly varying cross-section. *J. Fluid Mech.* **64**, 209–226.

Haselton, F. R. & Scherer, P. W. 1982 Flow visualization of steady streaming in oscillatory flow through a bifurcating tube. *J. Fluid Mech.* **123**, 315–333.

Jones, A. F. & Rosenblat, S. 1969 The flow induced by torsional oscillations of infinite planes. *J. Fluid Mech.* **37**, 337–347.

Lyne, W. H. 1970 Unsteady viscous flow in a curved pipe. *J. Fluid Mech.* **45**, 13–31.

Riley, N. 1965 Oscillating viscous flows. *Mathematika* **12**, 161.

Riley, N. 1967 Oscillatory viscous flows, review and extension. *J. Inst. Maths Applics* **3**, 419–434.

Rosenblat, S. 1959 Torsional oscillations of a plane in a viscous fluid. *J. Fluid Mech.* **6**, 206–220.

ROSENBLAT, S. 1960 Flow between torsionally oscillating disks. *J. Fluid Mech.* **8**, 388–399.

SCHERER, R. W. & HASELTON, F. R. 1982 Convective exchange in oscillatory flow through bronchial-tree models. *J. Appl. Physiol.: Respirat. Environ. Exercise Physiol.* **53**, 1023–1033.

SCHLICHTING, H. 1932 Berechnung ebner periodischer Grenzschichtstomungen. *Phys. Z.* **33**, 327–335.

SPECIAL CONFERENCE REPORT. 1983 High-frequency ventilation for immature infants. Report of a conference, March 2–4, 1982. *Pediatrics* **71**, 280–284.

STUART, J. T. 1966 Double boundary layers in oscillatory viscous flow. *J. Fluid Mech.* **24**, 673–687.

TARBELL, J. M., ULTMAN, J. S. & DURLOFSKY, L. 1982 Oscillatory convective dispersion in a branching network. *Trans. ASME* K: *J. Biomech. Engng* **104**, 338–342.

WEIBEL, E. R. 1963 *Morphometry of the Human Lung*. Academic.